OBSERVATIONAL CONSTRAINTS ON THE DIFFUSION OF COSMIC-RAY ELECTRONS IN SPIRAL GALAXIES

K. A. MARSH

Jet Propulsion laboratory MS 246-101
California institute of "1'ethnology
4800 Oak Grove Drive, Pasadena, CA 91109

AND

G. HELOU

Infrared Processing and Analysis Center
California Institute of Technology 100-22, Pasadena, CA 91125

I

Abstract

We have performed some quantitative tests of the "smearing" mode] for the radio emission in spiral galaxies. In this model, the infrared and radio emission are dominated by the effects of the formation and subsequent evolution of massive OB stars; the radio is produced by sync. chrotron emission from relativistic electrons accelerated during the supernova phase, and which are partially confined by the magnetic field of the galactic disk. Subsequent diffusion of these electrons causes the radio image to appear as a smeared version of the infrared image. We have tested the model for a set of nearby galaxies (24 spirals and 1 irregular), using a data set consisting of radio images (20 cm wavelength) and infrared images (60 pm wavelength) for which each radio/infrared pair had been processed to have the same spatial resolution (]'). Previous work has suggested that the smearing functions have exponential form, Some of the goals of our study were to examine this suggestion, and to determine the characteristic length scale for the smearing. Two different approaches were used, namely: (a) parametrized fits to exponential and Gaussian functions, and (b) deconvolution of the infrared image from the radio image, using a positivity constraint to increase the accuracy of the estimated kernel. Our conclusions are as follows:

(]) The radio images can be reproduced, to reasonable accuracy, by smearing the infrared images with compact (O- 6 kpc) positive-valued kernels, with residuals typically 10- 20% of the local radio intensity over a range of almost 2 orders of magnitude in radio intensity.

(2) In most (but not all) cases, an exponential] smearing function provides a better fit than a Gaussian.

(3) For the inclined galaxies (i.e., those whose galactic planes are tilted by more than $45°$ with respect to the sky plane), the smearing function is, in some cases, significantly elongated along the axis of tilt, while in other cases there is no significant elongation. The elongation tends to occur when the smearing scale exceeds 1 kpc, suggesting that the scale heights of the galactic disks are of this order. Furthermore, the elongated smearing functions tend to be better fit by exponentials rather than Gaussians, whereas the converse is true for the non-elongated functions. This behavior is consistent with diffusion and decay of cosmic-ray electrons when the confinement scale is less than the scale height of the galactic disks, and escape of the electrons for the larger scales.

(4) Departures from the simple Gaussian or exponential forms are due principally to elongations of the smearing kernels in directions other than the major axis of the galaxy, rather than to differences in the radial profiles of the kernels. They are therefore indicative of anisotropy, probably due to local variations in the magnetic field geometry.

in the analysis. Since the infrared-to-radio ratio map in Paper 1 showed that the NW component exhibited radial gradients while the SE component did not, the analysed region was confined to the NW component.

3 Convolutional Relationship

According to the smearing model, the true intensity distributions in radio and infrared are related via convolution with a smearing kernel $\kappa(\mathbf{r})$, where $\mathbf{r}$ is a 2-dimensional angular position vector whose components are the the right ascension and declination, and $\kappa(\mathbf{r})$ is normalized such that:

$$\iint \kappa(\mathbf{r})d^2\mathbf{r} = 1 \tag{1}$$

The observed radio and infrared images (denoted by $R(\mathbf{r})$ and $1(r)$, **respective] y**), represent convolutions of the true distributions with the point spread functions (1' SF's) of the respect ive measurement systems, which were closely matched by means of the processing discussed in Paper 1. Since the convolution operator is commutative, $R(r)$ and $I(\mathbf{r})$ would therefore be related by the same convolution kernel, $\kappa(\mathbf{r})$, as for the true distributions. in the absence of measurement noise and model error, we would thus have:

$$R(\mathbf{r}) = Q\text{-}^* \iint I(\mathbf{r}')\kappa(\mathbf{r} - \mathbf{r}')d^2\mathbf{r}' \tag{2}$$

where Q represents the ratio of total flux densities in infrared and radio.

4 Parameterized fitting Procedure

In this section we will examine the assumption that the smearing function can be represented adequately by either an exponential or a Gaussian function, and will determine the set of parameters which give the best fit to the data in each case.

4.1 Description of Technique

We will assume that the functional form of κ can be described by the two parameters ℓ and s, the first being a discrete-valued label (representing the function type), and the second being an appropriate] y defined scale length. The function types which will be considered here are:

$\ell = 1$: Gaussian, circular in plane of sky
$\ell =-- 2$: Exponential, circular in plane of sky
$\ell = 3$: Gaussian circular in plane of galaxy
$\ell = 4$: Exponential circular in plane of galaxy

We will define s to be the halfwidth of the function at the $1/c$ points. be the halfwidth of the function at the $1/c$ points. in those cases for which the function is assumed to be circular in the plane of the galaxy, $\kappa(\mathbf{r})$ involves the additional parameters i and θ, representing the inclination of the plane of the galaxy with respect to the plane of the sky, and the position

4

angle of the axis of tilt, respectively. In order to represent the functional dependence of κ more explicitly, we will use the notation $\kappa(\ell, s; r)$.

in practice, $R(\mathbf{r})$ and $I(\mathbf{r})$ are sampled on a discrete, regularly spaced grid of pixels, such that the jth pixel has location $\mathbf{r}_j$. For brevity, we will denote quantities such as $R(\mathbf{r}_j)$ by R_j. The discretized version of (2) is then:

$$R_j = Q^{-1} \sum_k \kappa_{jk}^{(\ell,s)} I_k \tag{3}$$

where

$$\kappa_{jk}^{(\ell,s)} = \kappa(\ell,\, s; \mathbf{r}_j - \mathbf{r}_k)/\Omega$$

and Ω is the solid angle subtended by the radio or infrared image.

Equation (3) is, of course, idealized. In practice there will be both measurement error and model error. We will assume that model errors predominate, and adopt a simple statistical model in which the standard deviation of the local model error is a constant, percentage of the local radio intensity. After allowance for such errors, (3) becomes:

$$R_j = Q^{-1}(1 + \eta_j) \sum_k \kappa_{jk}^{(\ell,s)} I_k \tag{5}$$

where η_j is a dimensionless quantity whose values are distributed according to a zero-mean Gaussian random process, The latter may be regarded as spatially uncorrelated provided the images are sampled appropriately (at intervals corresponding to the width of a resolution element or greater), and hence the covariance can be expressed as:

$$E\, \eta_j \eta_{j'} = \sigma_\eta^2 \delta_{jj'} \tag{6}$$

where σ_η is the standard deviation of the η_j values, E is the expectation operator, and $\delta_{jj'}$ is the Kronecker delta,

Taking the logarithm of Equation (5), we have:

$$\ln R_j = \ln \hat{I}_j(\ell,s) - \ln Q + \ln(1 + \eta_j) \tag{7}$$

where $\hat{I}_j(\ell,s)$ represents the jth sample of the convolved infrared image, i.e.

$$\hat{I}_j(\ell,\, s) = \sum_k \kappa_{jk}^{(\ell,s)} I_k \tag{8}$$

Since $\ln(1 + \eta_j) \simeq \eta_j$ for small η_j, we can rewrite (7') as:

$$\ln R_j = \ln \hat{I}_j(\ell,S) - \ln Q + \eta_j \tag{9}$$

On the basis of (9), maximum-likelihood estimates of ℓ, s, and Q (denoted by $\hat{\ell}, \hat{s}$, and $\hat{Q}$, respectively) can be obtained from the observed radio and infrared images by minimizing the sum of squares of residuals, $\phi(\ell, s, Q)$, given by:

$$\phi(\ell, s, Q) = \sum_j [\ln R_j - \ln \hat{I}_j(\ell,s) + \ln Q]^2 \tag{lo}$$

The variances in the estimated values of s and Q are given by the diagonal elements of γ^{-1}, where γ is a matrix whose elements represent the second derivatives of $\phi(\ell, s, Q)/(2\sigma_\eta^2)$ with respect to s and Q (Kendall & Stuart 1979). Since σ_η is not known a *priori*, we estimate it from the residuals of the fit, i.e.

$$\sigma_\eta^2 \simeq \frac{\phi(\hat{\ell}, \hat{s}, \hat{Q})}{N} \tag{11}$$

where N is the number of spatial samples.

Since ℓ is a discrete-valued quantity, its uncertainty is characterized by the relative probabilities of the possible values. Two probabilities of interest are P_{exp}, which represents the probability that the optimal convolving function is an exponential rather than a Gaussian, and P_{sky}, the probability that the optimal function is circular in the plane of the sky rather than in the plane of the galactic disk. If we assume:

1. The only possible function types are the four listed above.

2. Each function is equally likely *a priori*.

3. The choice between the Gaussian and exponential forms is completely independent of the choice between the sky-plane and disk-plane forms, a priori.

then the two probabilities are given by:

$$P_{exp} = \frac{1}{1 + \exp\left[-\frac{N}{2}\left(\frac{\phi_{gauss} - \phi_{exp}}{\phi_{min}}\right)\right]} \tag{12}$$

$$P_{sky} = \frac{1}{1 + \exp\left[-\frac{N}{2}\left(\frac{\phi_{gal} - \phi_{sky}}{\phi_{min}}\right)\right]} \tag{13}$$

where ϕ_{min} represents the minimum value of $\phi(\ell, s, Q)$ over all values of ℓ, and ϕ_{exp}, ϕ_{gauss}, ϕ_{sky}, ϕ_{gal} represent the minimum values over the restricted domains $\ell \in \{2, 4\}$, $\ell \in \{1, 3\}$, $\ell \in \{1, 2\}$, and $\ell \in \{3,4\}$, respectively. Two other probabilities related to those above are: $P_{gauss} = 1 - P_{exp}$ and $P_{gal} = 1 - P_{sky}$.

The physical usefulness of the estimated parameters depends on how well the model represents the data. One measure of this is the residual map, where the jth residual can be expressed as:

$$r_j = 111\left[\hat{Q}^{-1}\hat{I}_j(\hat{\ell}, \hat{s})\right] - \ln R_j \tag{14}$$

$$\simeq \frac{\hat{Q}^{-1}\hat{I}(\hat{\ell}, \hat{s})}{R_j} - 1 \tag{15}$$

From Equation (15), the ability of the model to reproduce the radio data from the infrared can be judged by comparing the residuals directly with the observed ratio maps (the infrared-to-radio intensity ratio as a function of position) as presented in Paper J.

An overall figure-of-merit for the fits is the RMS residual, given by:

$$RMS = [\phi(\hat{\ell}, \hat{s}, \hat{Q})/N]^{\frac{1}{2}} \tag{16}$$

Since from (15), each residual represents the fractional error between observed and modeled radio intensity, the RMS value from (16) may also be regarded as a fractional error.

6

4.2 **Results**

The results of the analysis, as applied to all of the data, are presented in Table 1. A 'G' or 'E' in column 1 denotes that the best-fitting function was a Gaussian or exponential, respectively. A subscript 's' or 'g' means that the best-fitting function was circular in the plane of the sky or the galaxy, respectively. Where no subscript is present, it means that the galaxy is close to being in the plane of the sky. A 'δ' in column 1 signifies that the best-fit,ting function was a delta function, i.e., smoothing with exponential or Gaussian functions of significant width did not improve the correspondence between the radio and infrared images.

The smearing scale listed in Table 1 represents the half-width at the 1/e points, along the major axis of the optimal smearing function, Two values of Q are listed, namely Q_{fit} (estimated using the least-sc~uares procedure) and Q_{global} (estimated from the integrated flux density in the radio and infrared images). Also listed in Table 1 are P_{exp} and P_{sky}, as defined above.

A comparison of the estimated smearing scales with the results of BH90 reveals that the present values are systematically smaller than those of BH90, typically by a factor of 2. There arc exceptions to this- in some cases, (e.g. NGC 4254 and NGC 51 94) there is agreement within the error bars of Table 1, while in others (e.g. NGC 55) there is strong disagreement, with the present value being an order of magnitude less than that of BH90. The discrepancies can probably be attributed to the superior spatial resolution of the present data, and/or the fact that the BH90 analysis may have been susceptible to numerical instabilities resulting from the simultaneous solution for smearing scale and galaxy size.

In order to investigate possible differences in the behavior of the estimated quantities as a function of position in the galaxy, the above analysis was repeated for the inner and outer regions of each galaxy. No significant difference was found between the estimated smearing scales for the two regions.

Finally, residual maps were produced; a representative set is shown in the column labelled 'a' in Figures 1-4, alongside a radio image of each galaxy. The fact that these residual maps show much less structure than the corresponding ratio maps of Paper 1 is qualitative evidence in support of the smearing model. Quantitatively, however, the residuals are much higher than the random noise associated with the radio and infrared maps; the noise is dominated by errors in the resolution-processed radio maps, which have a dynamic, range of approximately 70:1. The random noise in these images ranges from approximately 1.4% in the central region of the galaxy to about 33% at the edges of the regions plotted in the residual maps. Since the RMS values of the residual maps arc typically $\sim 25\%$, it is clear that the assumed model is inadequate in some way, For example, the assumed functional forms for the smearing function (exponential and Gaussian) may not be the correct ones, and/or other physical processes, besides the propagation of relativistic electrons, may be important for determining the radio intensity distribution, in order to assess this possibility, we have directly estimated the form of the smearing function using deconvolution, and the results arc described in Section 5.

Figure 5 shows a plot of smearing scale versus galaxy size, the latter being defined as the e-folding scale, ℓ_{disk}, of the best-fit of the infrared data to an exponential disk, values of which have been taken from Paper 1. From the figure, there appears to be an upper envelope

such that the e-folding scale of the smearing function is limited by thee-foldillg scale of the galactic disk, For $\ell_{disk} < 4$ kpc, the scale of the smearing function is typically half the scale of the disk.

On the question of the best form of the convolving function:

(1) 'l'able 1 shows that an exponential is preferred in 72% of the cases.

(2) 'l'able 1 also shows that in some cases, the best-fit function is circular in the plane of the sky, while in others it is circular in the plane of the galactic. disk, i.e. is elongated like the appearance of the galaxy as projected onto the plane of the sky. If we confine our attention to the more significant cases ($P > 0.7$, where P is the larger of P_{sky} or P_{gal}), then an interesting trend emerges when the results are compared with the exponential/Gaussian preference, as shown in Table 2. It is apparent that the preference for a function which is circular in the sky-plane is correlated with a preference for a Gaussian smearing function, and the preference for a function which is circular in the disk-plane is correlated with a preference for an exponential smearing function.

(3) In all but 1 of the cases for which the smearing function is circular in the plane of the sky, the smearing scale is < 1 kpc. Conversely, in all but 2 of the cases for which the smearing function is elongated along with the galaxy, the smearing scale is > 1 kpc. At first glance, this might seem like a resolution effect, whereby the smearing kernels of the most distant galaxies are spatially unresolved and therefore circular in the plane of the sky. If this were the case, however, the delineation between elongated and non-elongated galaxies would occur at a fixed angular scale rather than linear scale (a significant, distinction in view of the fact that the subset of inclined galaxies spans an order of magnitude in distance, whose range is 2.9- 25.7 Mpc [1)1190]). Furthermore the two galaxies with the strongest preferences for a function which is circular in the sky plane (NGC 55 and NGC 1569) also happen to be the two closest galaxies in the subset (3,2 and 2.9 Mpc, respectively). At such distances, elongation on scales ~ 1 kpc would have been easily detectable if present. This argues strongly for a non-instrumental origin for the effect.

5 Deconvolution Procedure

We now describe our deconvolution procedure., designed to estimate the true form of the smearing function, free from constraint s imposed by preconceived functional forms.

5.1 Description of Technique

Rearranging (2), we have:

$$R(\mathbf{r}) = Q^{-1} \iint I(\mathbf{r} - \mathbf{r'}) \; \kappa(\mathbf{r'}) d^2\mathbf{r'} \tag{17}$$

Since this is a convolutional relation, the function $\kappa(\mathbf{r})$ can, in principle, be estimated by deconvolving the observed infrared image from the corresponding radio image. Since deconvolution is a noise-vulnerable process, however, it must be carried out within the framework of an estimation procedure which takes full account of stochastic effects, which include both

measurement noise and model errors. Rewriting (17) in terms of quantities defined on a discrete grid of pixels, and making allowance for model error, η_j, and measurement noise, μ_j, we obtain:

$$R_j = Q^{-1}(1 + \eta_j) \sum_k I(\mathbf{r}_j - \mathbf{r}_k)\kappa_k + \mu_j \tag{18}$$

where κ_k represents the value of the smearing kernel at location $\mathbf{r}_k$, defined such that $\sum_k \kappa_k = 1$. If we represent the model error and measurement noise by uncorrelated Gaussian random processes which are statistically independent of each other, then the model error and measurement noise terms on the RHS of (18) can be lumped into a single nonstationary noise term whose local variance is given to a sufficiently good approximation by:

$$\sigma_j^2 = \sigma_\eta^2 R_j^2 + \sigma_\mu^2 \tag{19}$$

where σ_μ^2 represents the variance of measurement noise.

An important physical constraint on the estimated form of $\kappa(\mathbf{r})$ is that it be nonnegative everywhere. The proper incorporation of this prior information can greatly increase the performance of a deconvolution algorithm. An algorithm which accomplishes this in an optimal way is the so-called "Gaussian with positivity" (GP) algorithm described by Richardson & Marsh (1983), and applied to astronomical image deconvolution by Marsh et al. (1995). When applied to the solution of (18) above, the algorithm assumes an *a priori* statistical model for the κ_j in which the probability density is that of a Gaussian random process of variance σ_κ when $\kappa_j > 0$, and is zero when $\kappa_j \le 0$. On this basis, the technique yields the most probable set of κ_j conditioned on the observed radio and infrared images.

in implementing the GP algorithm, σ_μ was set at 1/70-th of the peak value of the radio image, consistent with the estimated dynamic range, and the local model error was taken as 10%, i.e. $\sigma_\eta = 0.1$. The final results are not sensitive to the latter value; in essence, the ratio σ_η/σ_μ controls the relative weighting given to the inner (high intensity) and outer (low intensity) parts of each galaxy. The quantity σ_κ was assigned a nomimal value corresponding to $1/B$ (where B is the area of a resolution element in pixels), and adjusted to produce a reduced chi squared value of unity, indicating consistency between the estimated smearing kernel and the data. The input data for the deconvolutions were selected in the same: way as for the parametrized estimation in Section 4, i.e., R_j values which occurred at the positions of confusing sources were eliminated.

In order to assess the spatial resolution of each estimated smearing kernel, each of the radio images was deconvolved from itself. It was found that the central peaks of the resulting images had dimensions (defined by the FWHM along minor and major axes) typically of 2 x 3 pixels, and hence the deconvolved smearing kernels have a resolution of this order. By comparison, images deconvolved using the standard Wiener filter approach (which does not employ a positivity constraint) were found to have a resolution which was about 50% poorer, and were also degraded by the presence of negative lobes due to Helmholtz-type ringing.

5.2 Results

The results of the deconvolution, for 16 of the 25 galaxies, are presented in the columns labelled 'b' and 'c' in Figures 1-4. In each case, the residual map is shown in 'b', and the

estimated kernel is shown at the center of the corresponding image in 'c'. Also shown for comparison, on either side of the estimated kernel, are the best-fit exponential and Gaussian functions (on the left and right, respectively) from the analysis of Section 4. One-dimensional profiles of the deconvolved kernels are shown in Figure 6, together with the best-fit exponential and Gaussian functions (shown dotted and dashed, respectively). Each profile represents a slice along the major axis of the galaxy, defined as the tilt axis for the inclined galaxies and the N-S direction for the remainder.

The galaxies excluded from Figures 1-4 and Figure 6 were:

(a) NGC 628- a low surface-brightness galaxy whose infrared and radio morphologies are qualitatively inconsistent with the smearing model. One characteristic is the lack of an identifiable radio nucleus.

(b) NGC 3031- this galaxy gave a poor quality deconvolution, with large residuals. Examination of the residual map showed much systematic structure which could not be accounted for by the smearing model. The behavior may be related to the presence of a Seyfert nucleus.

(c) NGC 55, 891, 1097, 1569, 4631, 5907- these galaxies gave clean solutions, with residuals similar to those of the galaxies in Figures 1-4. However, the estimated kernels were only marginally resolved, and hence the size scales of these kernels were dominated by instrumental resolution effects. Note that this was not a problem for the parametrized estimation process of Section 4, partly because the assumed functional forms constituted much stronger prior information than the positivity constraint used in the deconvolution, thus enabling greater spatial resolution, and partly because the uncertainties resulting from finite instrumental resolution were fully specified by the calculated error bars.

(d) IC 10- an irregular. Although the SE component is morphologically inconsistent with the smearing model, the NW component fits the model well, and the results are included in the discussion which follows.

The dimensions of the estimated kernels (half width at the $1/e$ points along the galaxy's major axis) are presented in Table 3, which includes the irregular galaxy, IC 10. These results may be directly compared with the smearing scales estimated from the parametrized procedure of Section 4. Such a comparison is presented in Figure 7, which shows consistency between the two sets of estimates.

Also included in Table 3 are the RMS residuals after allowance for measurement noise; specifically, these values represent *a posteriori* estimates of the fractional model error, σ_η, obtained from the residuals between the radio image and the smeared infrared image, after removing the estimated contribution of the constant term, σ_μ in (19). For comparison, the corresponding RMS residuals for the parametrized fits are listed alongside.

It is apparent that in many cases, the exponential/Gaussian forms have provided just as good fits as the deconvolved kernels. In other cases, however, the residuals after deconvolution are substantially less than those obtained from the parametrized fits. The three best examples are NGC 3621, NGC 4303, and NGC 5236, for which the difference is at least 0.1. Examination of the kernel shapes (see Figures 2 and 4) shows a substantial amount of extended structure. Furthermore, there is significant elongation of the kernels in all threw cases, despite the fact that two of the three galaxies (NGC 4303 and NGC 5236) are viewed nearly face-on ($i = 24°$ in both cases- BH90). There are other cases in which low-inclination

10

galaxies have significantly elongated smearing kernels. For example, NGC 3344 ($i = 20°$) and NGC 4254 ($i = 270$). The results suggest that anisotropy in the disk plane is an important factor in the diffusion process.

In order to look for evidence of *radial* anisotropy, (i.e., that the smearing has a preferred direction with respect to the galactic. center), the deconvolution analysis was repeated using subsets of the data, selected on the basis of azimuthal location. Specifically, the radio image for each galaxy was divided into 4 quadrants centered on the position of the central peak, and delineated by the N-S and E-W axes in the sky. The smearing function was then estimated separately for each quadrant and compared with the reference function (obtained by deconvolving the radio image from itself) in order to assess whether any quadrant-dependent differences were significant. No evidence for any radial anisotropy was found at a resolution of 1'.

We have also investigated the question of whether smearing functions other than exponentials or Gaussians would provide better fits to the data. Guided by the appearance of the profiles in Figure 6, we have tried triangular functions and truncated exponentials and Gaussians. In no case was the fit improved. The only function which produced a systematic improvement in the fits was one of the form $\kappa(r) = \exp[-(r/r_0)^{\frac{1}{2}}]$, which gives broader wings than either an exponential or a Gaussian. The improvement, however, was only modest (a decrease in the RMS residual of typically ~ 0.01).

6 Discussion

We have found that the radio images can be reproduced, to reasonable accuracy, by smearing the infrared images with relatively compact, positive-valued kernels. The residuals are typically 10-20% of the local intensity, over a range of almost 2 orders of magnitude in radio intensity. Furthermore, the simple, single-peaked morphology of the estimated smearing kernels is consistent with a process dominated by diffusion.

6.1 Comparison to Models

The median smearing length for the galaxies studied is about 1.05 kpc. More than a third of the sample galaxies (9 objects) have a smearing scale length between 0.6 and 1.2 kpc. This interval maps roughly to a range of 1 to 10 cm^{-3} in mean interstellar densities, using Figure 2 in 11}193, which assumes $h_0 = 100$ pc, $B \propto n^{1/2}$, and $\ell_{mfp} = 1$ pc$\left(\frac{n}{1\ cm^{-3}}\right)^{-1/3}$ for 10 GeV electrons. For these assumptions, the range of scale lengths observed marks the transition from cosmic ray electron (CRE) losses being dominated by escape to being dominated by synchrotron decay. Under the same assumptions, the smallest observed smearing lengths at less than 0.5 kpc imply yet higher mean interstellar densities in the galaxy.

'There is however an interesting trend related to the size of the smearing scale, namely that shorter smearing scales tend to be associated with Gaussian-shaped kernels, whereas exponential-shaped kernels tend to have the greater scale lengths. Indeed, except for NGC 7331, all Gaussian smearing kernels have scale lengths smaller than 1.2 kpc, and three out of the six have a scale ≤ 0.5 kpc. In addition, as pointed out in §4.2, Gaussian-shaped kernels

prefer 3-dimensional isotropy as opposed to the exponential-shaped kernels that tend to be flattened like the disk of the galaxy.

Thus smearing kernels are observed to become elongated in the galaxy disk and exponentially-shaped only once their scales exceed about 1 kpc, suggesting that this scale is typical of the scale heights of disks. Indeed, one would expect clouds of CRE to remain roughly spheric.al very early in their evolution, or if the magnetic field strength is so high as to make decay the dominant loss mechanism. As the CRE diffuse more than about one kpc, their distribution should flatten, reflecting the finite thickness of the galactic disk, and they should start escaping rather than decaying, thereby acquiring an exponential radial profile as argued by HB93.

If disk scale heights are indeed closer to 1 kpc than 100 pc, then we must re-examine the validity of our density estimate based on Figure 2 of HB93. However, since the scale height, h_0, used in that Figure describes the dust associated with interstellar gas rather than the radio disk thickness which we infer here, the density estimates remain valid, subject to the caveats expressed in HB93. The larger scale heights do however affect the parameters of the simple confinement model sketched out in §5 of HB93. In this model, the product $h_0^{-1} \times \epsilon_{esc}^{1/2}$ was required to be constant, with the escape probability of a cosmic ray at each visit to the disk boundary $\epsilon_{esc} \lesssim$ 10-3 for $h_0 =$ 100 pt.. If h_0 were increased to 1 kpc the escape probability would also have to be increased to roughly 0.] , probabl y a more reasonable confinement efficiency given the weak and fragmented magnetic field one would expect high above a galactic disk,

6.2 **Variation in convolution kernel**

The fact that significant residuals remain even after the use of the optimal smearing function (estimated by deconvolution) indicates that the relation between the infrared and radio continuum images of a galaxy is more complex than could be described by a simple smearing model. This complexity could arise in several ways, the simplest of which is that while the radio continuum is a smeared version of the infrared, the smearing kernel varies its size, shape, or both as a function of location within the galaxy.

The quadrant analysis in §5.2 rules out one limited case of shape variation, namely that the kernel might be elongated in a direction linked to the radial direction in the galaxy, Such an anisotropy is physically plausible given the strong radial density gradients in galaxy disks, yet it is not observed, The same density gradient. suggests as equally plausible a radial gradient in the size of the smearing kernel. This too is ruled out however by the results of the comparison of inner with outer disk regions in $4.2. Apart from systematic variations, the scale length of the smearing kernel is also sensitive to the age of the cloud of CRE responsible for the synchrotron emission, and to the local magnetic field strength and geometry, all of which are known to vary in galactic disks. This random variation may well be the main contributor to the residual discrepancies between the radio image and the smeared infrared image, and may in addition obscure any systematic trends across the disk.

Another possibility is that '(smearing') as described by convolution is an incomplete description of the relation between the two images, implying physical processes at work beside those considered in the HB model. We now discuss this possibility.

6.3 **Other smearing processes**

If- as assumed by HB---spreading, decay and escape are the dominant processes for radio emitting CRE, and the cosmic ray sources are coincident with massive stars, then convolution is an appropriate transformation from the infrared to the radio continuum images of a galaxy. That transformation however may not be adequate if significant contributions are made by other processes, such as reacceleration of CRE far from their original sources. The results of Paper I, especially that Q peaks only at the intensity peaks, argue that reacceleration cannot be a dominant process, but do not rule it out entirely. If reacceleration is due to diffuse shocks in the interstellar medium, then the relation between infrared and radio might still be amenable to description by a convolution, albeit with a flat-topped or at most centrally depressed kernel. We therefore cone.]ucle that if reacceleration is the cause of the residuals under discussion, it is more likely to be linked to localized features such as spiral density waves or supernova shocks, as this would lead to more variation in the radio emission profiles around cosmic ray sources.

Another possibility is that a significant fraction of CRE escape through breaches in the disk associated with superbubbles or other accidents, rather than in a distributed, steady-state mode. The convolution description would be rendered inadequate by "sudden" partial escapes at random locations.

7   Acknowledgement

Table I: Parameter-estimation results

Galaxy	Best func.	RMS resid.	smearing scale [kpc]	Q_{global}	Q_{fit}	P_{exp}	P_{sky}
IC 10	E	0.245	0.15 ± 0.08	368	345 ± 30	0.646	
NGC 55	E_s	0.322	0.234-0.12	192	1903.22	0.649	0.983
NGC 253	G_g	0.471	0.32 ± 0.95	173	1453.24	0.468	0.459
NGC 628	E	0.425	4.24 ± 6.21	220	2045-31	0.660	
NGC 891	E_g	0.139	1.053.0.48	94	89 ± 4	0.542	0.355
NGC 1097	E_g	0.120	1.02 ± 0.16	117	127 ± 5	0.569	0.253
NGC 1569	G_s	0.117	0.203 0.04	116	112 ± 6	0.456	0.957
NGC 2403	G_s	0.259	0.504 0.21	259	239 ± 22	0.485	0.740
NGC 2903	G_s	0.133	1.20 ± 0.15	141	134 ± 8	0.465	0.858
NGC 3031	E_s	0.633	0.743.1.36	134	153 ± 34	0.907	0.563
NGC 3344	E	0.210	1.104.0.39	128	121 ± 9	0.725	
NGC 3556	E_g	0.242	2.39 ± 0.70	113	102 ± 9	0.760	0.000
NGC 3621	E_g	0.347	2.013 0.88	133	1334.16	0.735	0.119
NGC 4254	E	0.308	2.24 ± 0.81	82	80 ± 9	0.770	
NGC 4303	E	0.411	4.97 ± 3.28	147	144 ± 21	0.587	
NGC 4490	E_g	0.183	1.04 ± 0,27	62	56 ± 4	0.763	0.001
NGC 4565	E_g	0.256	0.86 ± 3.14	92	87 ± 8	0.500	0.498
NG C 4631	G_s	0.317	0.99 ± 0.40	73	61 ± 7	0.471	0.732
NGC 5055	E_s	0.272	0.673.0.28	127	111 ± 11	0.590	0.757
NGC 5194	E	0.236	1.95 ± 0.87	86	89 ± 7	0.886	
NGC 5236	E	0.272	0.724.0.41	114	118 ± 11	0.797	
NGC 5907	δ	0.184		158	164 ± 7		
NGC 6946	E	0.294	0.713.0.41	97	88 ± 9	0.895	
NGC 7331	G_g	0.198	4.473.0.68	92	88 ± 7	0.355	0.000
NGC 7793	E_s	0.413	0.474 0.39	213	210 ± 31	0.634	0.679

Table 2: Comparison between forms of the best-fit smearing function

'-Circular in sky plane $(P_{sky} > 0.7)$		Circular in disk plane $(P_{gal} > 0.7)$	
Galaxy	Best func.	Galaxy	Best func.
NGC 55	E	NGC 1097	E
NGC 1569	G	NGC 3556	E
NGC 2403	G	NGC 3621	E
NGC 2903	G	NGC 4490	E
NGC 4631	G	NGC 7331	G
NGC 5055	E	---	

Table 3: Deconvolution results

Galaxy	Smearing scale [kpc]	RMS residual Deconvolved:	model error Fitted:
IC 10	0.140 '-'	0 . 2 1 9	0.172 '
NGC 253	0.535	0.540	0.550
NGC 2403	0.449	0.142	0.182
NGC 2903	1.925	<0.014	< 0.014
NGC 3344	0.590	0.188	0.127
NGC 3556	2.337	0.166	0.157
NGC 3621	2.707	0.096	0.308
NGC 4254	2.296	0.405	0.244
NGC 4303	2.757	0.282	0.517
NGC 4490	2.300	<0.014	<0.014
NGC 4565	5.567	0.107	0.100
NGC 5055	1.588	0.03)	0.130
NGC 5194	1.362	0.209	0.193
NGC 5236	0.738	0.037	0.182
NGC 6946	0.699	0.217	0.247
NGC 733 I	4.657	0.030	0.055
NGC 7793	0.473	0.286	0.352

8 References

Aumann, 11. 11., Fowler, J. W., and Melnyk, M. IWO, AJ, 99, 1674

Bicay, M. D. and Helou, G. IWO, ApJ, 362, 59

Condon, J. J. 1987, ApJS, 65, 485

Helou, G. & Bicay, M. D. B. 1993, ApJ, 415, 93

Kendall, M. and Stuart, A. 1979, "The Advanced Theory of Statistics Vol. 2: Inference and Relationship," (London: Charles Griffin).

Marsh & K. A., Helou, G, 1995, ApJ, 445, 599

Marsh, K. A., Van Cleve, J. E., Mahoney, M. J., Hayward, 'I'. 1,., & Houck, J. R. 1995, ApJ, 451, 777

Richardson, J. M. & Marsh, K. A. 1983 Proc. SPIE, 413, 79

Figure Captions

Figures 1--4: Residual maps ant] estimated kernels, presented with with the radio images for comparison, with a field of view of 15' x 15' in each case. The left hand plot in each case shows the 20 cm radio image on a logarithmic scale of 2 decades; the plots in the column labelled 'a' show the residuals of the fit of the radio data after the parameter-fitting procedure, and those in the 'b' column show the residuals after deconvolution. The residuals are defined as:

$$\ln[\text{scaled-and-convolved infrared}] - \ln[\text{radio}]$$

and are plotted with a range of --1.0 to + 1.0 in each case, such that black is positive and white is negative.

The estimated smearing kernels are shown on a linear scale in the column labelled 'c'. The central kernel represents the results of deconvolution, while the left ant] right kernels represent the best-fit exponential and Gaussian functions, respectively, for comparison.

Figure 5: Plot of smearing scale versus galaxy size, using smearing scales estimated from parametrized fits.

Figure 6: Profiles of estimated smearing kernels, along the major axis of each galaxy. The solid lines represent the kernels estimated by deconvolution; the clotted and dashed lines represent the results of parametrized fits, corresponding to exponentials and Gaussians, respectively.

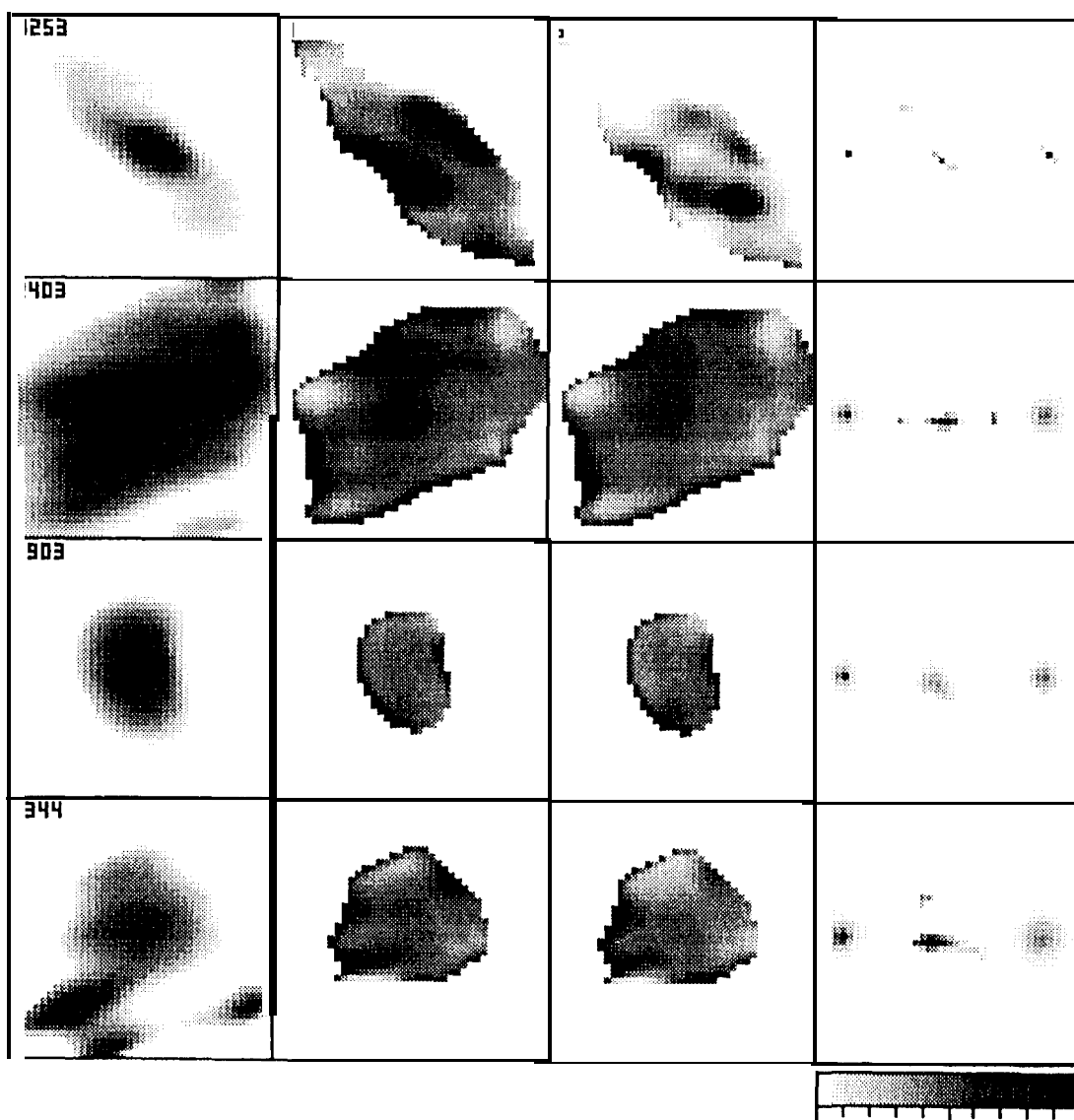**Figure** 7: Comparison of smearing-scale estimates based on parametrized fits (vertical scale) versus deconvolution (horizontal scale).
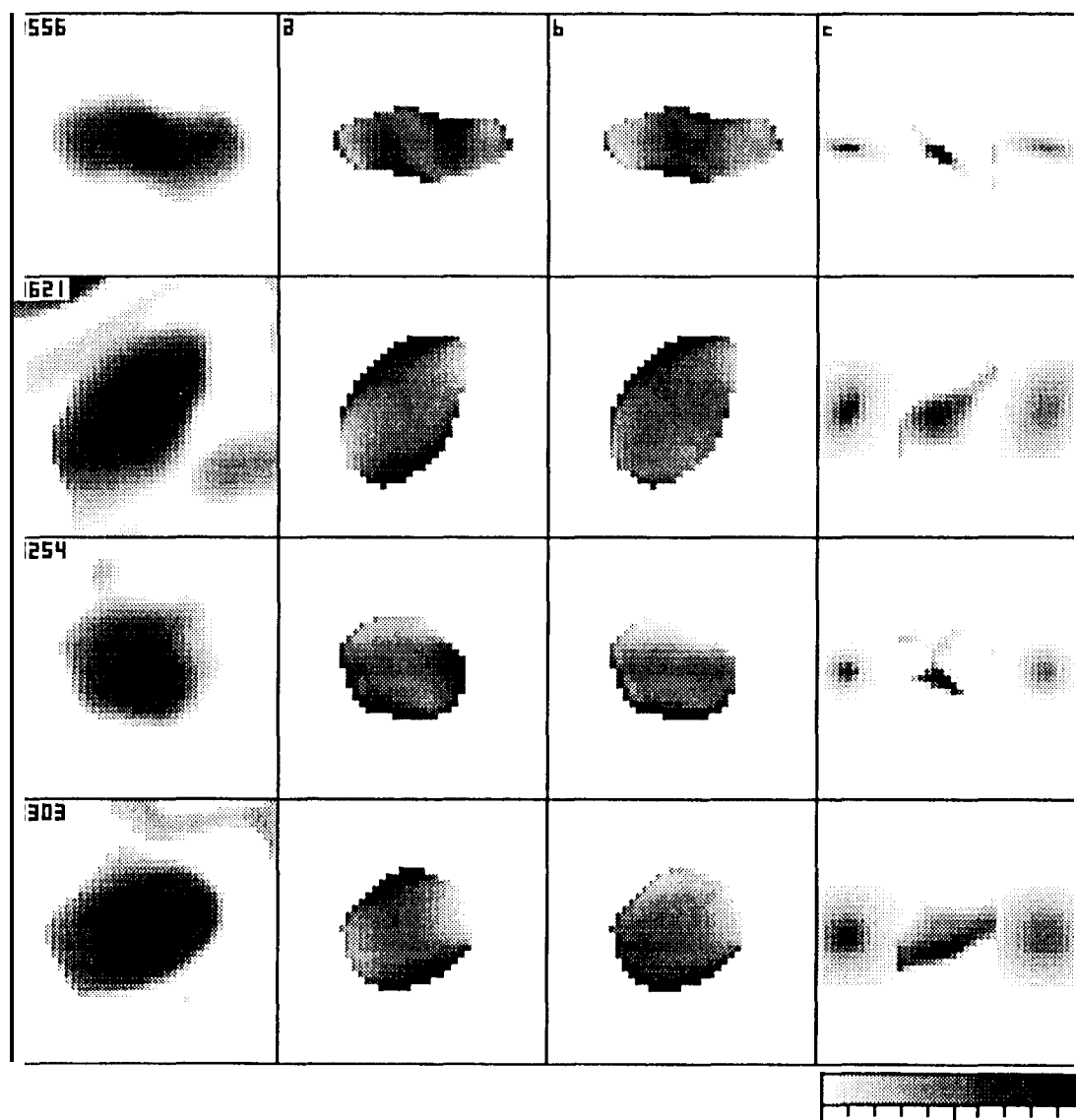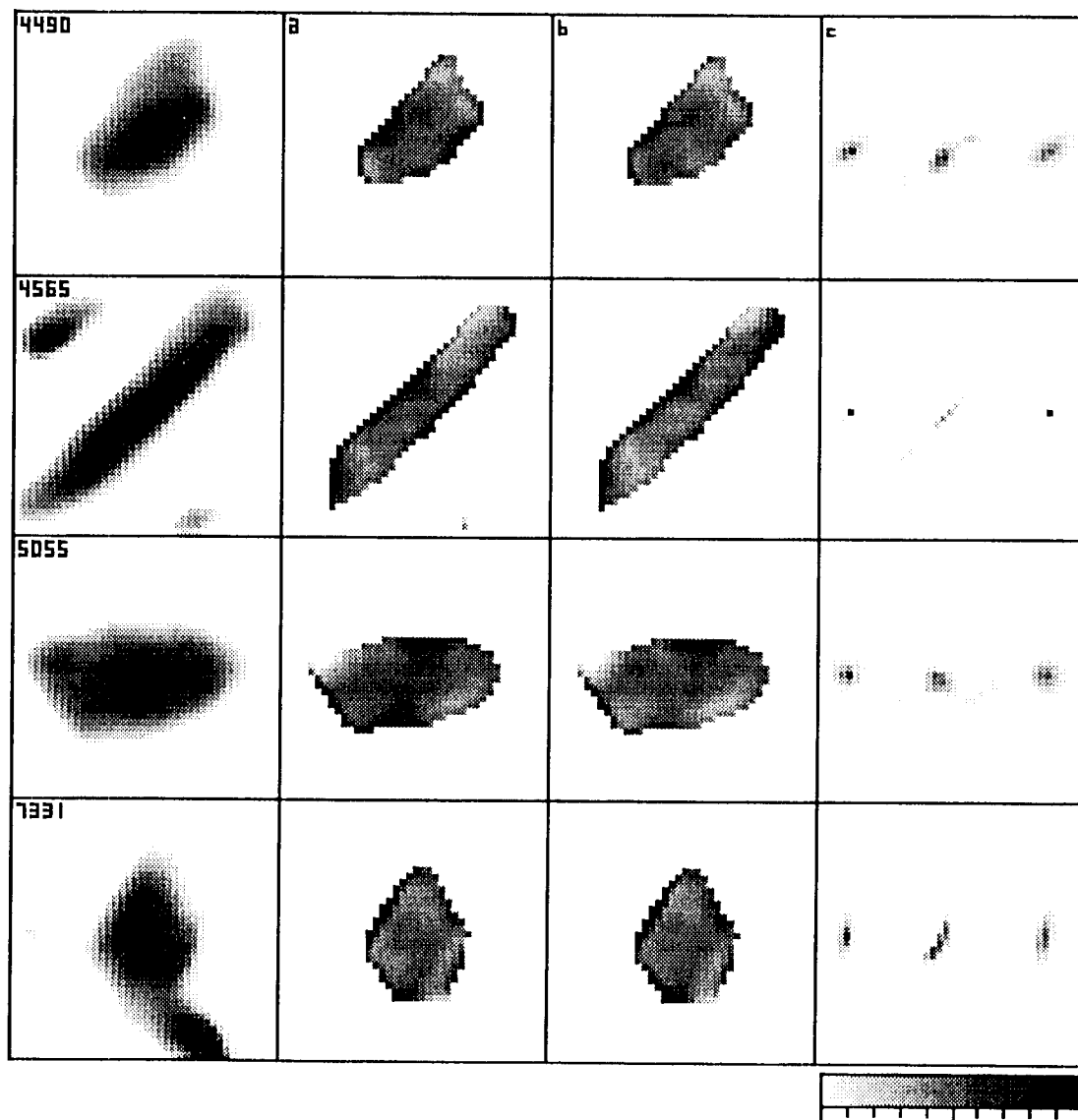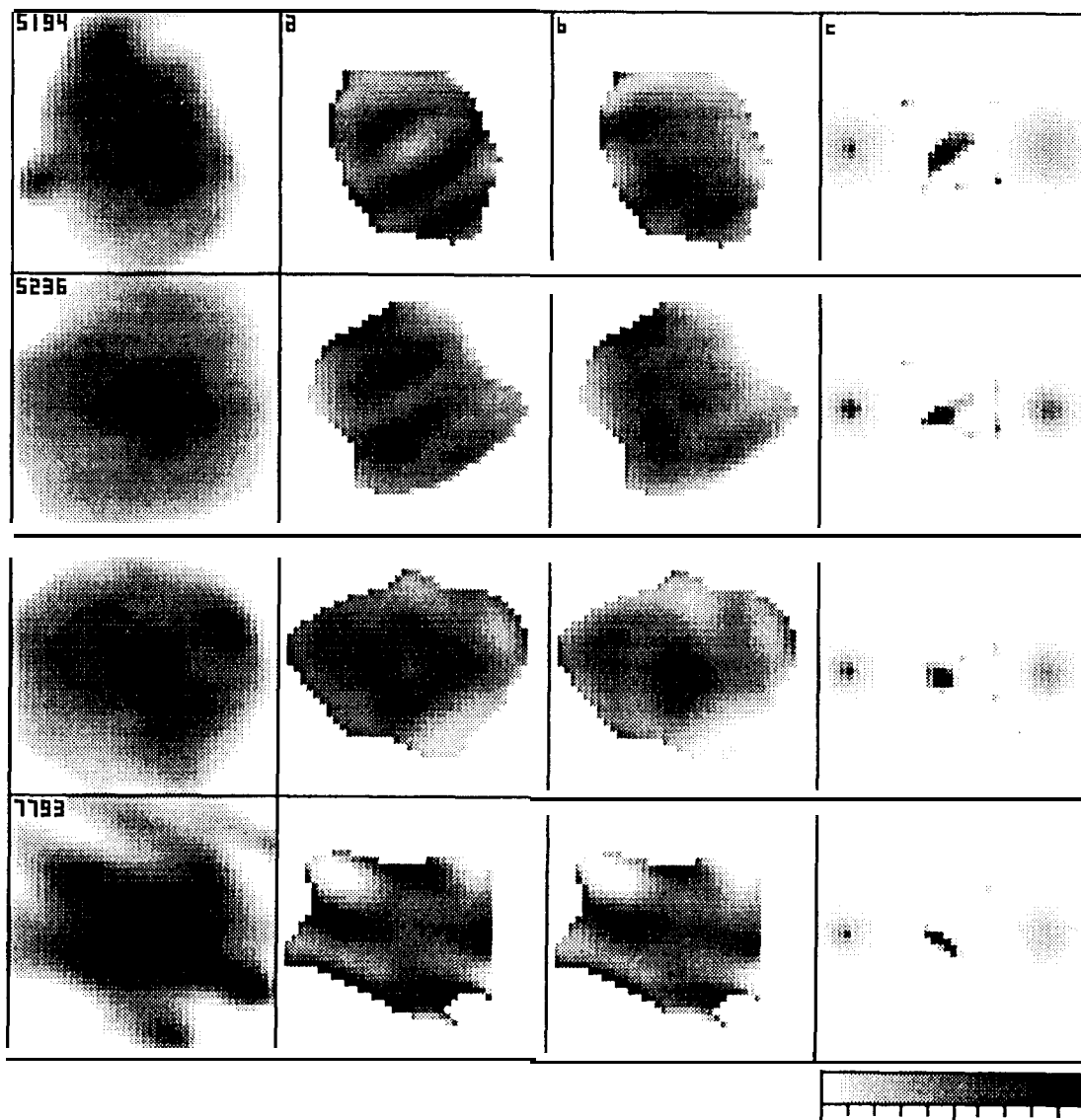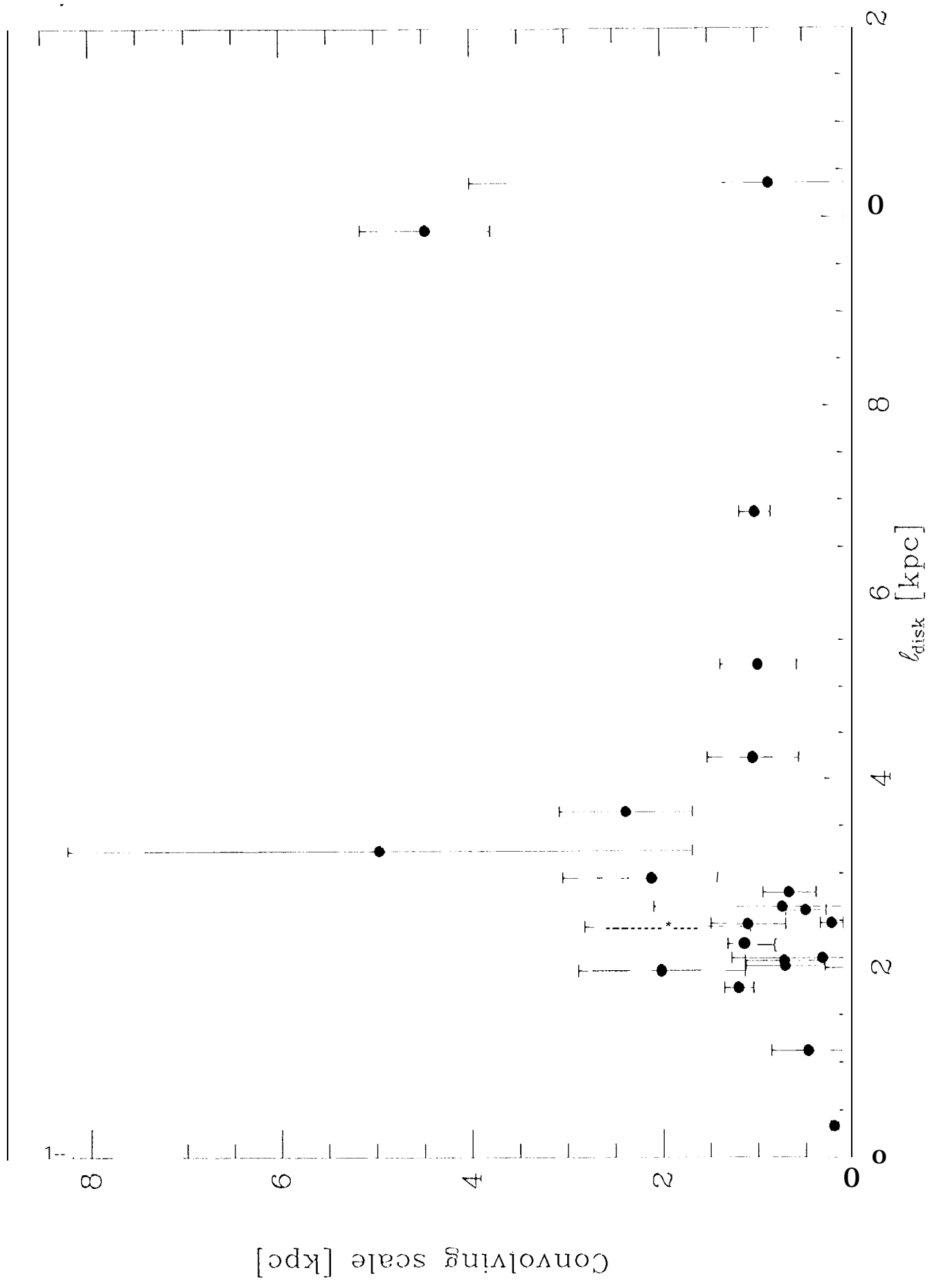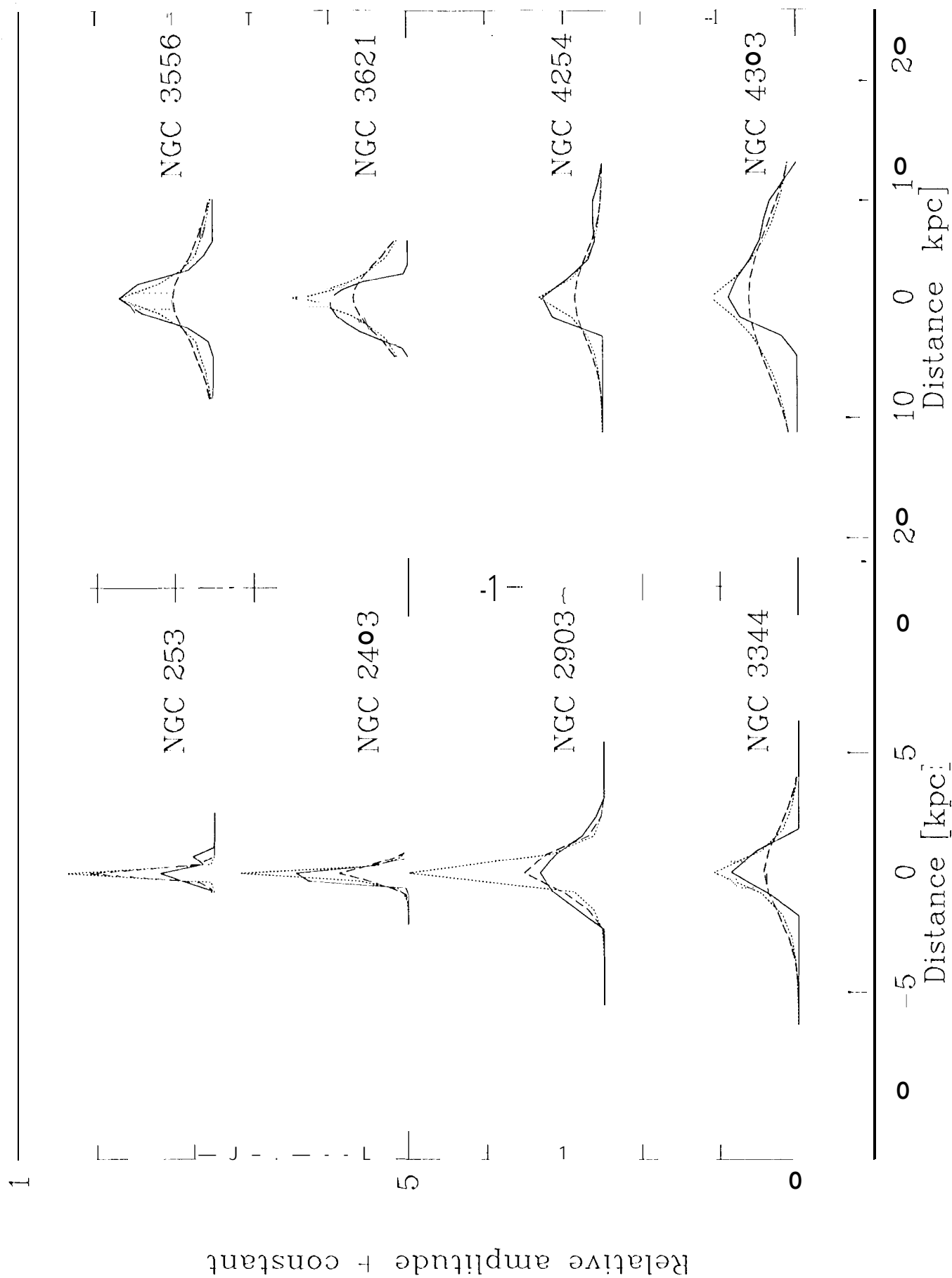
Figure 1

Figure 2

Figure 3

Figure 4

Fig 5

Fig 6a

Fig b

Scale estimated from fit [kpc]

Scale of deconvolved image [kpc]

Fig 7